Steam reforming of methanol on binary Cu/ZnO catalysts: Effects of preparation condition upon precursors, surface structure and catalytic activity

Guo-Cheng Shen [a,b,*], Shin-ichiro Fujita [a], Susumu Matsumoto [a], Nobutsun Takezawa [a]

[a] *Department of Chemical Process Engineering, Hokkaido University, Sapporo 060, Japan*
[b] *Department of Chemistry, University of Toronto, 80 St. George Street, Toronto, Ont., Canada M5S 3H6*

Abstract

Precursors for Cu/ZnO catalysts, with Cu/Zn molar ratios in the range from 100/0 to 0/100, were prepared by two coprecipitation methods. These methods differ by the addition rate of a mixed $Cu(NO_3)_2/Zn(NO_3)_2$ solution to a $NaHCO_3$ solution. Characterisation by powder X-ray diffraction (PXRD), differential thermal analysis (DTA), thermal gravimetric analysis (TGA), FT-IR and UV/VIS spectroscopies indicated that the structure of precursors with Cu/Zn ratios in the range of 30/70 to 70/30 depends greatly upon the addition rate of the mixed solution. Amorphous copper hydroxycarbonate and sodium zinc carbonate were formed prior to the various precursors such as malachite, aurichalcite and hydrozincite. The Cu/ZnO catalysts subsequently formed from the precursors showed the activity for steam reforming of methanol to vary with its composition. Based on the results of temperature programmed oxidation (TPO) with N_2O and an infrared spectra of CO chemisorption, the TOF of the reaction is proposed to be associated with the surface of metallic Cu.

Keywords: Malachite (M), $Cu_2CO_3(OH)_2$; Hydrozincite (H), $Zn_5(CO_3)_2(OH)_6$; Aurichalcite (A), $(Cu,Zn)_5(CO_3)_2(OH)_6$; Sodium zinc carbonate (SZC), $Na_2Zn_3(CO_3)_4$; Temperature programmed oxidation (TPO); Turnover frequency (TOF)

1. Introduction

Steam reforming of methanol has been developed with high selectivity and high activity on copper-containing catalysts [1–3]. In our previous work, the reaction was carried out on catalysts prepared by kneading hydroxides of copper with various metal oxides and by exchanging copper (II) cations with the protons of surface hydroxyls on silica [3,4]. The catalytic

activation of the reaction requires copper that is highly dispersed on a support. However, the extent of dispersion of copper was restricted using the above two preparation methods. Recently, coprecipitation/characterization of a binary Cu/ZnO catalysts have been developed for the purpose of highly dispersed copper [5–11].

In this report, Cu/ZnO catalysts with various Cu/Zn molar ratios were prepared from a mixed $Cu(NO_3)_2/Zn(NO_3)_2$ solution that was added to a $NaHCO_3$ solution. Cu–Zn hydroxycarbonates and their reduced products were character-

* Corresponding author. E-mail gshen@chem.utoronto.ca

ized by PXRD, DTA, TGA, FT-IR and UV/VIS spectroscopies and TPO, CO chemisorption. The mechanism of precursor formation and effective catalysis of the surface of metallic Cu for the steam reforming of methanol are also discussed.

2. Experimental

2.1. Catalyst preparation

Precursors for Cu/ZnO catalysts with Cu/Zn molar ratios in a range from 100/0 to 0/100 were prepared by two coprecipitation methods. These differ by the addition rates of a mixed $Cu(NO_3)_2/Zn(NO_3)_2$ solution to a $NaHCO_3$ solution [12]. 50 ml of mixed $Cu(NO_3)_2/Zn(NO_3)_2$ solution (1.0 M) was added dropwise to 100 ml of $NaHCO_3$ solution (1.2 M, pH 8.2) over 90 min (denoted method A) or 20 min (denoted method B) at 338 K with stirring. The precipitates formed were further aged for 90 min under continuous stirring, then filtered, washed with deionized water and dried at 373 K overnight. The precipitates were denoted as S_{An} or S_{Bn}, where A or B signifies the method employed and n signifies the mole fraction of Cu to total Cu and Zn multiplied by 10.

The precursor was calcined at 623 K in air for 4 h, followed by reduction in a stream of 3% H_2 and 97% He at 483 K for 1 h. The temperature was then raised to 523 K by 10 K/h and finally kept at 523 K for 1 h in pure H_2, to give the S_n-derived Cu/ZnO catalyst.

2.2. Temperature programmed oxidation (TPO) of the Cu / ZnO catalysts with N_2O

After the reduction, the Cu/ZnO with adsorbed H_2 was flushed with He at 553 K for 20 min. The temperature was lowered to 223 K under He and then switched to a steam of 2% N_2O and 98% He at 100 cm^{-3} STP/min. The TPO run was carried out in a U-shaped flow reactor from 223 to 723 K at a heating rate of 3 K/min. The effluent from the reactor was analyzed by gas chromatography.

2.3. Reaction

Steam reforming of methanol was carried out in a flow system from 413 to 563 K at atmospheric pressure, where 40 mg of the Cu/ZnO catalysts was loaded. An equimolar mixture of methanol and water was admitted by a microfeeder and rapidly vaporized in a nitrogen stream before entering the catalyst bed. The total inflow rate was kept at 100 cm^3 STP/min. The partial pressure of either methanol or water was kept at 0.24 atm in an inlet of the catalyst bed. The reactants and products in outflow were determined by two gas chromatographs (Hitachi Model 023 and Yanagimoto Model G-1800) with a thermal conductivity detector.

2.4. Characterization of the samples

The precursor, intermediate precipitate and the Cu/ZnO catalysts were characterized by PXRD, UV-visible, DTA, TGA and diffuse reflectance FT-IR spectroscopies and CO chemisorption. The PXRD measurements were carried out using a Rigaku ADP-310E with Ni-filtered Cu radiation [$\lambda(K\alpha) = 1.5418$ Å]. UV-visible spectra were recorded on a Hitachi-330 spectrometer with a photomultiplier detector. DTA and TGA experiments were performed on Rigaku 8441A and Hitachi-50 analyzers, respectively, in which the samples were heated under a N_2 atmosphere at a rate of 5°C/min. The FT-IR spectra of the samples were recorded by a Jasco-5M spectrometer with 50–100 coadded scans at 2 cm^{-1} resolution. The quantities of the various precursors present in the precipitate were determined based on the integrated intensities of PXRD or DTA peaks of the samples.

3. Results and discussion

3.1. Characterization of the precursor

The precursor structure was determined by PXRD and DTA. Fig. 1a illustrates the PXRD

patterns of precursors prepared by method A. S_{A10}, S_{A9}, S_{A7} and S_{A5} show only the characteristic pattern of malachite, $Cu_2CO_3(OH)_2$ [13]. The peaks of malachite in S_{A9}–S_{A5} samples are broadened with increasing Zn content (Fig. 1a, lines 2–4). In contrast, the PXRD pattern for S_{A0}, S_{A1} and S_{A3}, show hydrozincite $[Zn_5(CO_3)_2(OH)_6]$ [14] (Fig. 1a, lines 5–7). With a careful inspection of Fig. 1a, lines 5–7, the characteristic peaks of hydrozincite in S_{A1} and S_{A3} are not broadened significantly, in comparison with pure hydrozincite in S_{A0}. The reflection of malachite decreases in intensity, whereas the reflection of hydrozincite increases, with increasing zinc content (Fig. 1a, lines 5–7).

Fig. 1b illustrates the PXRD patterns of precursors prepared by method B and shows a moderate difference from those of method A in Cu/Zn ratios of 70/30 to 10/90. S_{B7} and S_{B5} show the pattern of aurichalcite, $(Cu, Zn)_5(CO_3)_2(OH)_6$ [15], and malachite (Fig. 1b, lines 3 and 4). S_{B3} shows only the pattern of aurichalcite (Fig. 1b, line 5). On the other hand,

S_{B10} and S_{B9} show the pattern of malachite (Fig. 1b, lines 1 and 2), while S_{B1} and S_{B0} show the pattern of hydrozincite (Fig. 1b, lines 6 and 7).

The structure of pure malachite has been determined by Well et al. who found a distorted octahedral coordination around cupric ions [16]. It is interesting to note that zinc can be doped into the malachite lattice, giving zincian-malachites [17,18]. Porta et al. [8] calculated the lattice parameters a, b, c, β and the cell volume (v) of zincian-malachites and showed that the cell volume of the zincian-malachites decreases with increasing zinc content. Our PXRD peaks determined that S_{A9}, S_{A7}, S_{A5} and S_{B9} ascribed to the monoclinic malachite structure, but with peaks which broaden with increasing Zn content. This seems indeed in contrast with expectations based only on the isomorphous substitution of Cu^{2+} by Zn^{2+} ions within the malachite lattice, since the octahedral ionic radii for Cu^{2+} and Zn^{2+} are 0.73 and 0.74 Å, respectively [19,20]. The decrease of the cell volume
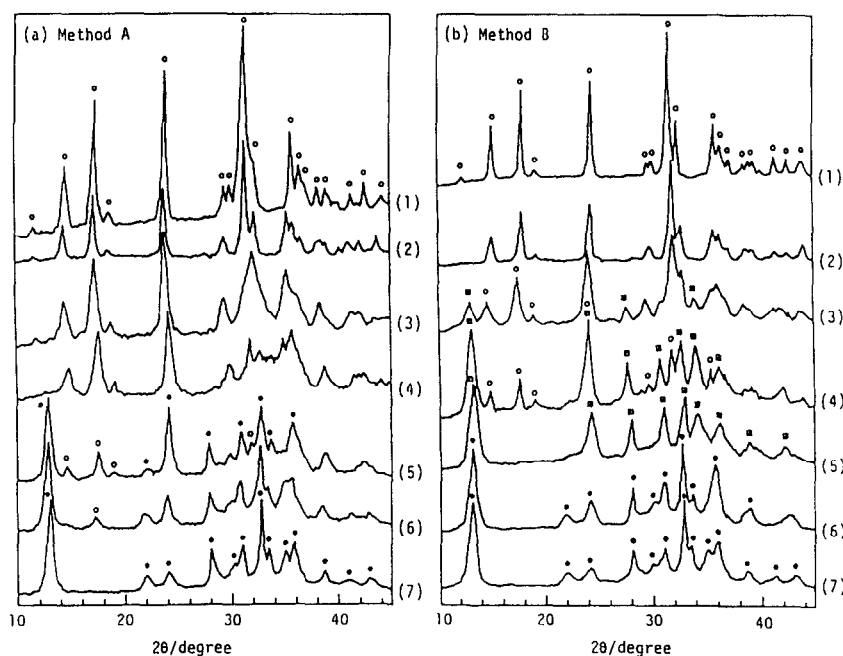

Fig. 1. PXRD patterns of the precipitates. (a) Prepared by method A, (b) Prepared by method B. (1) Cu/Zn = 100/0, (2) 90/10, (3) 70/30, (4) 50/50, (5) 30/70, (6) 10/90 and (7) 0/100. ○, malachite or zincian-malachite; ●, hydrozincite or copper-hydrozincite; ◼, aurichalcite.

and the broadened behavior of the PXRD peaks for zincian-malachites, may be explained by an increasing covalency of the metal–oxygen bond and/or by less octahedral site distortion around the metal atoms when zinc substitutes for the copper ions. Both effects lead to lattice shrinking and the lower crystallinity of the zincian-malachite than those of the pure malachite [8].

It is not surprising that beyond a certain limit of solubility of Zn into the malachite, such as S_A with Zn content higher than 50% and S_B with Zn content higher than 70%, a new phase, hydrozincite is observed (Fig. 1a, lines 5–7 and Fig. 1b, lines 6–7). S_{A5}, S_{A6} and S_{B6} are considered as being copper-containing hydrozincite phase and as being the isomorphous substitution of Zn^{2+} by Cu^{2+} ions within the hydrozincite lattice. In spite of the fact that Cu^{2+} radius is shorter than Zn^{2+} radius, the covalent effect of Cu–O has more tendency than Zn–O, to give elongation of the oxygen octahedra [19,20]. The effects of these two opposing factors can not result in a significant variety in the characteristic peaks and in the lattice volume between copper-containing hydrozincite and pure hydrozincite (Fig. 1a, lines 5–7 and Fig. 1b, lines 6–7). On the other hand, for S_B with Zn content higher than 10%, in addition to the zincian-malachite phase, a new phase richer in zinc, i.e. aurichalcite starts to segregate (Fig. 1b, lines 3–5). Aurichalcite is the complex sheet structure which contains 60% octahedral and 40%
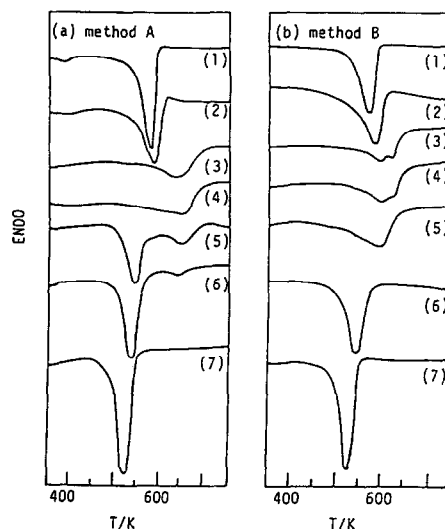

Fig. 2. DTA curves of the precipitates. (a) Prepared by method A, (b) Prepared by method B. (1) Cu/Zn = 100/0, (2) 90/10, (3) 70/30, (4) 50/50, (5) 30/70, (6) 10/90 and (7) 0/100.

tetrahedral sites for divalent cations [8,21]. Regardless of the fact that they have similar PXRD patterns, aurichalcite can be distinguished from hydrozincite, as has been demonstrated previously by Himelfarb et al. [7] and by means of a careful comparison for some X-ray reflections of these two chemically related compounds (Fig. 1b, lines 3–7). The distinction of all Cu, Zn hydroxycarbonates is listed in Table 1.

Fig. 2 shows the DTA curves of the precursors. In agreement with PXRD observations, DTA curves vary with Cu/Zn ratio and preparation methods. S_{A10} and S_{B10} decompose with

Table 1
The distinction of Cu, Zn hydroxycarbonates

Formula	rosasite	zincian-malachite	aurichalcite	hydrozincite
Symbol	R	Zn–M (Cu/Zn = 77/23)	A	H
Crystal system	monoclinic	monoclinic	orthorhombic	monoclinic
Space group	$P2_1/a$	$C2/m$	$B22_12$	$C2/m$
Unit cell dimensions (nm)				
a_0	0.940	0.942	2.720	1.358
b_0	1.230	1.208	0.641	0.628
c_0	0.340	0.320	0.529	0.541
β	90°	97°		95°35'
Distinguishable PXRD peaks of Cu, Zn hydroxycarbonates	14.7°, 17.3°	31.4°, 24.1°, 11.9°	34.1°, 41.9°	47.5°
Ref.	[22,23]	[8], our work	[24], our work	[24], our work

a sharp peak maximum at 576 K, to give CuO, irrespective of the preparation method (Fig. 2a, line 1 and Fig. 2b, line 1). This confirms that S_{A10} and S_{B10} are composed of pure malachite [8,25]. With an increase of the zinc content to 50%, the peak at 576 K broadens and shifts to a higher temperature (Fig. 2a, lines 2–4 and Fig. 2b, lines 2–4), suggesting that zincian-malachites were formed, as reported by Porta et al. [8,9,25]. S_{A0} and S_{B0} decompose with a sharp peak maximum at 525 K, to give ZnO (Fig. 2a, line 7 and Fig. 2b, line 7), indicating that S_{A0} and S_{B0} are comprised of pure hydroz-incite. The peak at 525 K shifts to higher temperature with increase of Cu content (Fig. 2a, lines 6–5 and Fig. 2b, line 6), suggesting that copper-hydrozincites were formed [8]. On the other hand, S_{B3}, S_{B5} and S_{B7} containing au-richalcite were detected by a peak in the DTA at 600–614 K, transforming to CuO and ZnO (Fig. 2b, lines 5–3) [8,26].

The composition of the precipitates was determined on the basis of the results of PXRD and DTA data. The variation of the composition of precursors with Cu/Zn ratio is summarized in Fig. 3. The composition of the precipitates with Cu/Zn ratios of 30/70 to 70/30 depends greatly upon the preparation method i.e. the addition rate of mixed $Cu(NO_3)_2/Zn(NO_3)_2$ solution to $NaHCO_3$ solution.

The decomposition temperature of our pure malachite agrees well with the mineral malachite [8,27]. A shift of the endothermic maxima from 576 to 652 K of the zincian-malachite phase (Fig. 2a, lines 2–4), agrees with the broadened peak and the shrinkage of the cell volume as observed by PXRD. This indicates that the dissolution of zinc in the malachite lattice induces the thermal stabilization of the structure. Moreover, the DTA analysis further confirmed that biphase, M/H in S_{A3} and S_{A1} samples (Fig. 2a, lines 6–7), M/A in S_{B7} and S_{B5} samples, as well as A/H in S_{B1} sample (Fig. 2b, lines 3–5) are present.

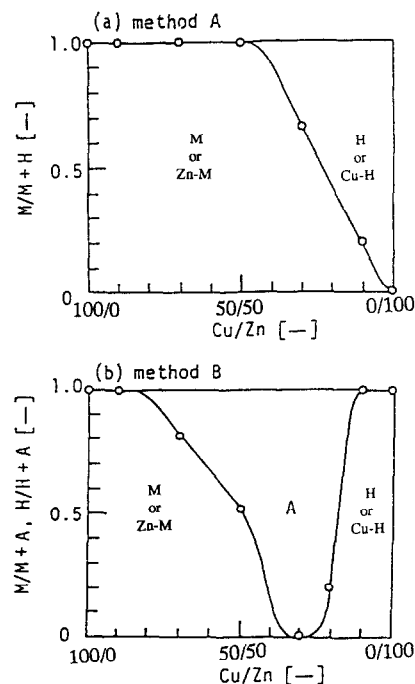On the other hand, the maximum peak temperature of pure hydrozincite showed a much

Fig. 3. Variation of the composition of precipitates with Cu/Zn ratio. (a) Precipitates were prepared by method A, (b) by method B. M, H and A represent malachite, hydrozincite and aurichalcite, respectively. The composition is in molar fraction.

lower temperature, 525 K (Fig. 2a, line 7 and Fig. 2b, line 7), in fair agreement with the decomposition temperature of 503 K given for this mineral [27]. A shift of the endothermic maxima from 525 to 550 K of the copper-hy-drozincite phase is observed with increasing Cu content. This suggests that the thermal stability of the zinc hydroxycarbonates increases with increasing copper content. The thermal stability of the Cu, Zn hydroxycarbonates could also be inferred from their standard free energies, ΔG° [28].

3.2. The mechanism of the precursor formation

To confirm the effect of the addition rate to the composition of precipitate, the precipitate, S_{A10} and S_{B10} with pure copper were sampled from $Cu(NO_3)_2$. By PXRD, DTA and FT-IR spectra analyses, it was found that the structure of the Cu-containing precipitate was markedly affected by the addition rate of $Cu(NO_3)_2$. The
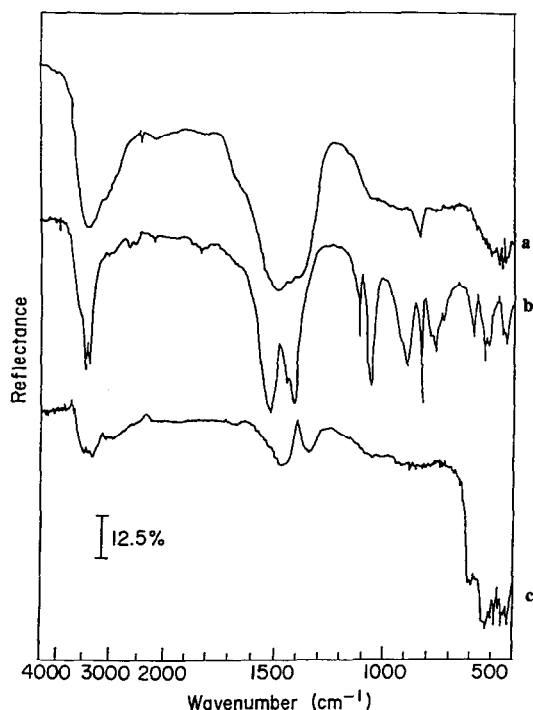
Fig. 4. (a) FT-IR spectra of the amorphous precipitates, prepared first in 4 min by method B; (b) FT-IR spectra of malachite; (c) FT-IR spectra of $Cu(OH)_2$.

precipitates showed the typical PXRD pattern of malachite at various stages of S_{A10} preparation. In contrast, during the initial stage of S_{B10} preparation, the precipitate showed a PXRD pattern of an amorphous material. Fig. 4 shows FT-IR spectra of this amorphous material, as well as malachite and $Cu(OH)_2$. The strong absorption bands of the amorphous material are present at 1480, 1370 and 835 cm^{-1} (Fig. 4, line a), indicating that carbonate species were present and the float band of O–H deformation at 1000–1100 cm^{-1} is similar with that of $Cu(OH)_2$. Moreover, GC and PXRD confirmed that the amorphous material decomposed to CuO, CO_2 and H_2O. These results suggest that the amorphous precipitate is Cu-containing hydroxycarbonates and is the intermediate between malachite and $Cu(OH)_2$.

TGA measurement (not shown) of the amorphous precipitate at different stages of S_{B10}

preparation, confirmed that amorphous $Cu(OH)_2$ was initially formed with rapid addition of $Cu(NO_3)_2$ solution, then being transformed to an amorphous copper hydroxycarbonate through the anion ligand exchange:

$$2Cu(OH)_2 + xCO_3^{2-} \rightarrow Cu_2(OH)_{4-2x}(CO_3)_x$$
$$+ 2xOH^- \qquad (1)$$
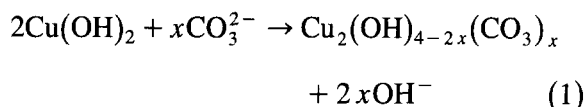
Upon aging, two OH^- ligands were exchanged by one CO_3^{2-} ligand and PXRD showed the formation of malachite, $Cu_2(OH)_2CO_3$ [12].

Similar experiments were carried out for the precipitates with other Cu/Zn ratios. The PXRD patterns showed the presence of malachite and sodium zinc carbonate, $Na_2Zn_3(CO_3)_4$ [29], in the initial stage of S_A preparation. Sodium zinc carbonate was converted gradually with time to hydrozincite [31]. On the other hand, during S_{B7}, S_{B5} and S_{B3} preparation, PXRD showed the presence of sodium zinc carbonate and the absence of copper-containing species in the initial stage. However, the precipitate showed a strong UV absorption at 800 nm, ascribed to Cu (II) species in octahedral sites, suggesting that the copper-containing species is amorphous as the initial stage of S_{B10}. It was found that sodium zinc carbonate initially formed, converted gradually with time to pure aurichalcite (S_{B3}) or malachite and aurichalcite $(S_{B5}$ and $S_{B7})$ [12,30].

A mechanical mixture of the amorphous material from $Cu(NO_3)_2$, and sodium zinc carbonate from $Zn(NO_3)_2$, was allowed to stand in a $NaHCO_3$ solution at 338 K. The mixture was found to convert to aurichalcite. In contrast, substitution of the amorphous material by malachite in such a system, sodium zinc carbonate was merely transformed to hydrozincite; no aurichalcite was detected by PXRD and DTA. When hydrozincite is used instead of sodium zinc carbonate, the amorphous material was converted into malachite, while hydrozincite remained unchanged. These findings strongly sug-

Method A

$$Cu^{2+} \longrightarrow M \longrightarrow M$$

$$Zn^{2+} \longrightarrow SZC \longrightarrow H$$
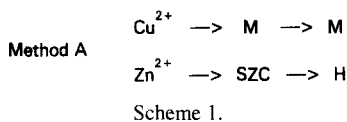
Scheme 1.

gest that aurichalcite was formed through a reaction of the amorphous material and sodium zinc carbonate.

Based on these results, the mechanism of precursor growth is proposed in Schemes 1 and 2. Slower addition results in the formation of malachite and sodium zinc carbonate (Scheme 1); rapid addition results in the formation of a copper-containing amorphous material and sodium zinc carbonate (Scheme 2) in the initial stage. In this way, sodium zinc carbonate transforms to hydrozincite and malachite remains unchanged (method A), while amorphous copper hydroxycarbonate competitively reacts with carbonate ions and sodium zinc carbonate, transforming to malachite and aurichalcite (method B), respectively, in the final precipitates.

3.3. Characterization of the Cu / ZnO catalysts by TPO run

The oxidation of the copper surface with N_2O,

$$N_2O(g) + 2Cu_S \rightarrow (Cu\text{-}O\text{-}Cu)_S + N_2(g) \qquad (2)$$
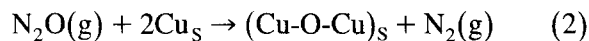
(where s denotes surface atoms), is a well-known method for measuring the copper surface area of supported copper catalysts [31,32]. By the characterization of ultraviolet photoelectron spectroscopy, Narita et al. [33] confirmed that the metallic Cu surface sites were transformed to monovalent Cu by the oxidation with N_2O at temperatures below 373 K. Habraken et al. [34,35] carried out the decomposition of N_2O on
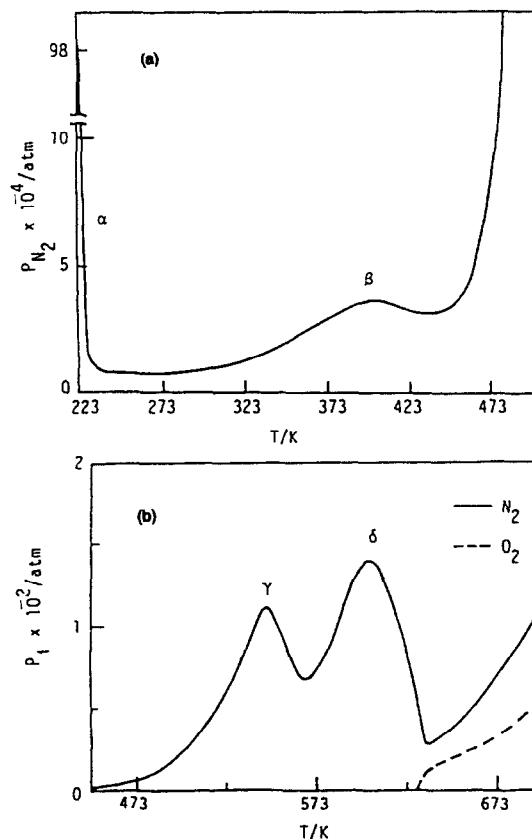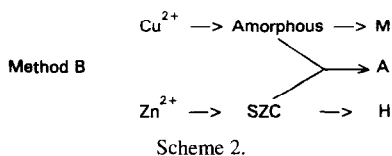
Method B

$$Cu^{2+} \longrightarrow Amorphous \longrightarrow M$$
$$\longrightarrow A$$
$$Zn^{2+} \longrightarrow SZC \longrightarrow H$$

Scheme 2.

Fig. 5. A profile of N_2 formation in the TPO run carried out on S_{A3}-derived Cu/ZnO catalyst. (a) The profile between 223 and 473 K; (b) the profile between 453 and 700 K.

Cu (111), Cu (110) and Cu (100) single crystal surfaces, finding great difference in the reactivity between these Cu surfaces and N_2O. In this regard, our research focuses on developing this method to determine surface structure of metallic Cu of the Cu/ZnO catalysts by oxidation of N_2O during a TPO run.

Fig. 5a shows profiles of N_2 formation in a TPO run on S_{A3}-derived Cu/ZnO catalyst. Upon feeding N_2O at 223 K, N_2 instantly forms and then rapidly decreases with temperature (α-N_2). A second peak of N_2 formation appears at 400 K (β-N_2). Above 450 K, the N_2 pressure increases significantly.

Fig. 5b shows two peaks (γ- and δ-N_2) of N_2 at 545 and 600 K. Beyond 633 K, O_2 is evolved. The partial pressure of O_2 in the effluent is one

half that of N_2, indicating that N_2O decomposition,

$$N_2O \rightarrow N_2 + 1/2O_2, \qquad (3)$$

took place. Based on these findings, one can consider that N_2O decomposed to four types of oxygen species, corresponding to the α-, β-, γ- and δ-N_2 in the TPO run, respectively. These oxygen species chemisorbed on metallic Cu, completely converting copper to copper oxide during the TPO run from 223 to 633 K. The amount of the oxygen species is the same as that of N_2. The four types of oxygen species were designated as α-, β-, γ- and δ-oxygen, respectively.

When the TPO run was carried out on S_{A0}-derived ZnO, a trace amount of N_2 was detected above 650 K. The formation of N_2 was exceedingly slower as compared with that on S_{A3}-derived Cu/ZnO catalyst. This strongly suggests that N_2 formation proceeded on the copper sites of the Cu/ZnO catalyst.

The total amount of α-, β-, and γ- oxygen species was practically the same as that of δ-oxygen species and the amount of all oxygen species was in good agreement with that of the oxygen required for conversion of metallic Cu to CuO. PXRD measurement of S_{A3}-derived Cu/ZnO was recorded to confirm the different stages of the TPO run. For the TPO run to 400 K, where α-, and β-oxygen species predominated, the PXRD pattern of metallic Cu and ZnO were observed. This suggests that α- and β-oxygen species were formed on the surface and/or sub-surface of metallic Cu, as in Eq. (2). For the TPO run up to 563 K (γ-oxygen species forming), the PXRD pattern revealed that metallic Cu converted to Cu_2O. For the TPO run to 630 K (δ-oxygen species forming), the PXRD pattern showed that the peak of Cu_2O diminished and the peak of CuO grew considerably. These prove that γ-oxygen species are due to the oxidation of bulk metallic Cu to Cu_2O,

$$N_2O + Cu_b \rightarrow (Cu\text{-}O\text{-}Cu)_b + N_2 \qquad (4)$$
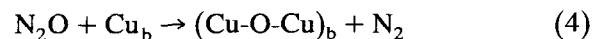
(where b denotes bulk Cu atoms) and that δ-

oxygen species are ascribed to the oxidation of Cu_2O to CuO,

$$(Cu\text{-}O\text{-}Cu)_b + N_2O \rightarrow 2CuO + N_2. \qquad (5)$$
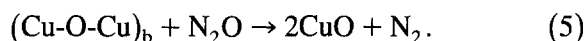
Similar TPO profiles were observed for N_2 formation on S_{A10}-S_{A1} and S_{B10}-S_{B1}-derived Cu/ZnO catalysts. Table 1 lists the amount of α- and β-oxygen species and the surface area of metallic Cu. Assuming spherical copper particles and 1.7×10^{19} atoms/m^2Cu [36], the average crystallite sizes of metallic Cu, $d(1)$ and $d(2)$ were estimated from the amount of α-oxygen species and the total amount of α- and β-oxygen species, respectively (Table 1). In Fig. 6a and b, the estimated values are com-
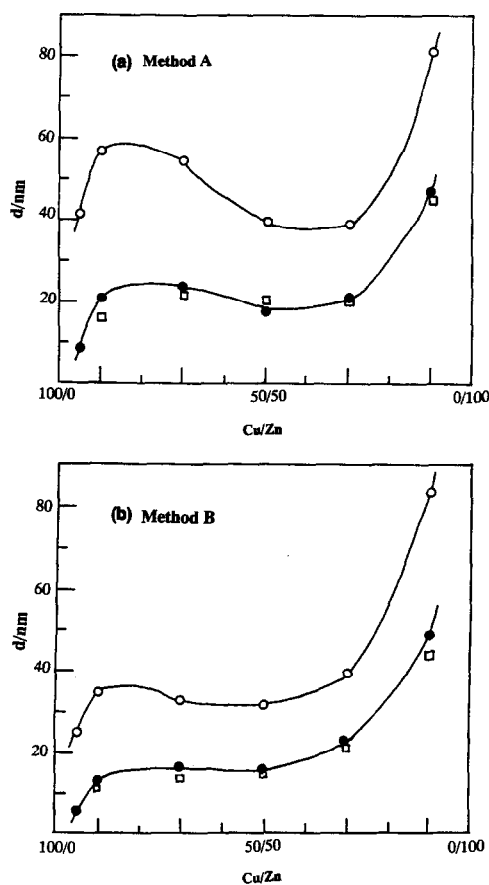

Fig. 6. Comparison of the average copper crystallite size. (a) Method A, (b) method B. $\bigcirc$, $d(1)$ and $\bullet$, d (2) were estimated from the amount of α-oxygen species and the total amount of α- and β-oxygen species, respectively; $\square$, were determined by PXRD.

pared with those measured by PXRD. The $d(2)$ values are well in agreement with the Cu crystallite sizes measured by PXRD.

Bartley et al. [37] and Luys et al. [38] claimed that the surface and sub-surface oxidation of copper simultaneously occurred at 363 K during N_2O decomposition. If β-oxygen species are formed on the Cu sub-surface, the $d(1)$ values of Cu crystallite size should correspond with those measured by PXRD. However, this does not hold in the present experiment, suggesting that both α- and β-oxygen species were formed on the Cu surface.

Scholten et al. [39] and Sengupta et al. [40] reported that oxidation of the bulk metallic Cu with N_2O occurred at temperatures higher than 373 K, where the β-peak was observed. They carried out the oxidation for 12 h, whereas, in the present TPO run, the temperature was raised from 373 to 423 K in 17 min. Therefore, the ascription of bulk Cu oxidation to the β-peak is not reasonable. On the other hand, Chinchen et al. [41] described that the surface oxidation of Cu was completed at 333 K by the determination of the frontal chromatography. However, with careful inspection of Fig. 2 in Ref. [41], N_2 was still formed at a slow rate after the breakthrough of N_2O. This slow evolution of N_2 would correspond to the β-peak in the present TPO run.
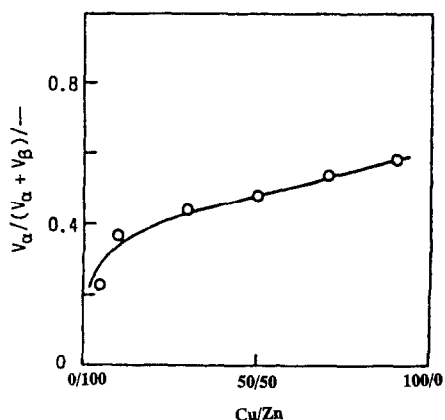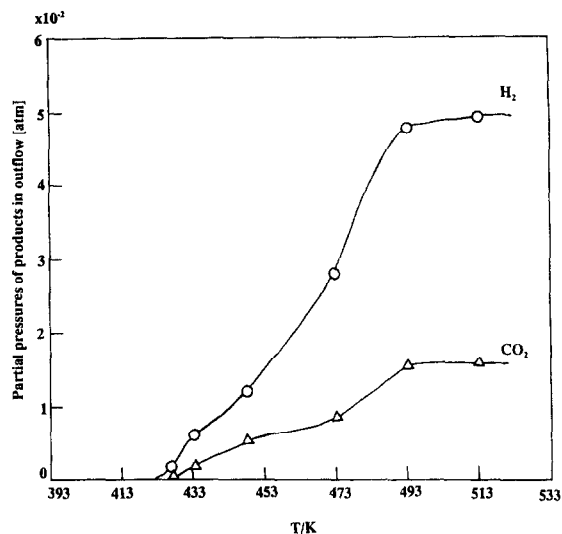

Fig. 8. Plot of particle pressure of products in the outflow against the temperature on the S_{A3}-derived Cu/ZnO catalyst.

The ratio of the amount of α-oxygen species (V_α) to the total amount of α- and β-oxygen species $(V_\alpha + V_\beta)$ against the Cu/Zn ratio is plotted in Fig. 7, in which the $V_\alpha/(V_\alpha + V_\beta)$ ratio increases with the Cu/Zn ratio, up to 90/10.

3.4. Steam reforming of methanol

Fig. 8 shows the plot of partial pressure of products against the temperature on the S_{A3}-derived Cu/ZnO catalyst. Carbon dioxide and hydrogen are the major products. The partial pressure of carbon monoxide and methyl formate was found to be far less than 10^{-5} atm and was therefore neglected. When the methanol–water mixture was admitted to the S_{A3}-calcined Cu/ZnO catalyst, the reaction initially proceeded at a fairly slow rate around 428 K, but gradually increased as hydrogen was evolved. Once the catalyst was completely reduced, a steady state of the reaction was rapidly attained which can be maintained for 20–25 h. An obvious feature is that the H_2 and CO_2 pressures quickly increase with increasing temperature and the increasing rate of formation tends to slow and becomes constant as tempera-

Fig. 7. Plot of $V_\alpha/(V_\alpha + V_\beta)$ against Cu/Zn ratio of the Cu/ZnO catalysts.

ture rises above 500 K. The ratio of H_2/CO_2 was the parameter indicative of selectivity, decreasing with increasing temperature.

The effect of the reaction temperature on the activity, selectivity and stability established that 493 K was the optimum operating temperature. Table 2 lists methanol conversion, rate and turnover frequency of H_2 at steady state conversion. The kinetic parameters on $Cu(OH)_2/SiO_2$-derived catalyst [3] are also listed for comparison. S_{A10}, M-derived Cu catalyst exhibits the lowest methanol conversion, 0.80%, and the lowest H_2 rate, 14.5 cm^3 STP/min g Cu. The methanol conversion substantially increases from 0.80% on S_{A10}, M-derived catalyst to 7.1% on S_{A9}, Zn–M-derived catalyst and the rate of H_2 formation correspondingly grows from 14.5 to 146 cm^3 STP/min g Cu. On the zincian-malachite precursor, S_{A9}- and S_{A5}-derived catalysts show methanol conversion to grow from 7.1 to 10.6% and the H_2 rate increases from 146.0 to 434.5 cm^3 STP/min g Cu with increasing zinc content. On S_{A3} (65%M + 35%H) and S_{A1}(20%M + 80%H)-derived Cu/ZnO catalysts, with decreasing M composition from 65 to 20%,

methanol conversion decreases from 6.8 to 1.0% and the H_2 rate reduces from 485.5 to 227.8 cm^3 STP/min g Cu. S_{A0}, H-derived Zn catalyst showed no activity for steam reforming of methanol.

The Cu/ZnO catalysts derived from S_{B10}, S_{B9} and S_{B1} show practically the same methanol conversion and H_2 rate as S_{A10}, S_{A9} and S_{A1}-derived catalysts. S_{B7}(80%M + 20%A) and S_{B5}(50%M + 50%A)-derived Cu/ZnO catalysts, show 11.2 and 12.9% methanol conversion, respectively. Comparing those with S_{A7} and S_{A5}, Zn–M-derived Cu/ZnO catalysts, it was interestingly found that a catalyst derived from the A-containing precipitate, displayed a H_2 rate enhanced by 8–22%. It is further notable that S_{B3} with A-derived Cu/ZnO catalyst shows a H_2 rate of 653.4 cm^3 STP/min g Cu, revealing an enhancement of 34.6% compared to that on S_{A3} (65% M + 35% H)-derived catalyst and being about 14 times of the activity of $Cu(OH)_2/SiO_2$-derived catalyst. The maximum activity of pure A-derived Cu/ZnO catalyst would be ascribed to fine interdispersion of Cu and ZnO during the treatment of precursor A. The activation energy of the reaction and the

Table 2

Surface area and dispersion degree of metallic Cu, amount of α- and β-oxygen species and kinetic parameters for steam reforming of methanol on various Cu/ZnO catalysts

Cu/Zn (mole ratio)	Method	Precursor composition (%)	MeOH conv. [a] (%)	R_{H2} [a] (cm^{-3} STP/ming Cu)	TOF [a] (s^{-1})	Amount of α-oxygen species [b]	Amount of β-oxygen species [b]	Dispersion degree (%)	Surface area (m^2/g Cu)
100/0	S_{A10}	M	0.80	14.5	1.10	0.20	4.68	0.08	0.35
	S_{B10}	M	0.84	15.2	0.60	0.22	9.23	0.12	0.67
90/10	S_{A9}	M	7.10	146.0	0.27	102.3	74.5	3.13	14.3
	S_{B9}	M	7.50	153.4	0.29	99.8	72.4	3.05	14.0
70/30	S_{A7}	M	10.3	288.6	0.24	156.0	133.9	6.63	31.9
	S_{B7}	80M + 20A	11.2	311.2	0.27	156.0	120.6	6.33	30.4
50/50	S_{A5}	M	10.6	434.5	0.32	105.2	111.9	6.99	35.1
	S_{B5}	50M + 50M	12.9	529.7	0.33	132.3	128.9	8.49	42.3
30/70	S_{A3}	65M + 35H	6.8	485.5	0.46	43.7	55.3	5.34	28.0
	S_{B3}	A	9.1	653.4	0.42	72.8	74.9	7.96	41.7
10/90	S_{A1}	20M + 80H	1.0	227.8	0.19	13.3	22.8	5.88	32.0
	S_{B1}	80A + 20H	1.1	241.5	0.12	22.0	37.9	9.74	53.1
30/70 (Cu/SiO$_2$) [c]	–	–	0.67	48.2	0.05	–	–	–	28.0

[a] Data obtained at 493 K.
[b] In unit of μmol/g cat.
[c] Ref. [3].

ratio of H_2/CO_2 were practically kept at approximately 20 kcal/mol and 3.1, respectively, irrespective of the preparation method and catalyst composition.

On the other hand, the TOF of H_2 was estimated from the atoms of metallic Cu and the H_2 rate. As shown in Table 2, S_{A9}, S_{A7}, S_{A5}, S_{A3} and S_{A1}-derived Cu/ZnO catalysts exhibit the TOF of 0.27, 0.24, 0.32, 0.46 and 0.19 s^{-1}, respectively, which is a significant decrease from 1.10 s^{-1} on support-free Cu catalyst. Similar features for the TOF of H_2 on S_{B10}–S_{B1}-derived Cu/ZnO catalysts are also observed in Table 2.

3.5. Infrared spectra of CO chemisorbed on the Cu / ZnO catalysts

Infrared spectra of the Cu/ZnO catalysts under CO chemisorption were investigated. As shown in Fig. 9, line g, the spectrum of S_{A0}-derived ZnO exhibits a single band at 2188 cm^{-1}, which is fundamental CO adsorption on ZnO [42]. In contrast, the spectrum of S_{A10}-derived Cu (Fig. 9, line a) shows another single band at 2100 cm^{-1}, ascribed to CO adsorbed on the surface sites of metallic Cu [43]. For S_{A9}, S_{A7}, S_{A5}, S_{A3} and S_{A1}-derived catalysts, in addition to the band at 2100 cm^{-1}, new bands emerge at 2090 cm^{-1} (Fig. 9, lines b–f) and 2170 cm^{-1} (Fig. 9, lines c–e). These bands at 2100, 2090, 2170 and 2188 cm^{-1} also appeared on S_{B10}–S_{B0}-derived Cu/ZnO catalysts.

Pritchard et al. extensively studied the infrared spectra of CO adsorption on various single crystal faces of copper [43–46]. They indicated that CO bands at 2102–2106 cm^{-1} and 2081–2090 cm^{-1} arise from CO adsorption on Cu(110) and Cu(100) surface, respectively [43,44], concluding that the absorption 2102–2106 cm^{-1} arise from CO adsorbed at steps or defects [44,46]. Here, CO adsorption at 2100 and 2090 cm^{-1} strongly suggests that the surface fraction of metallic Cu has steps or defects and flat sites. The absorption at 2100 cm^{-1} increases in relative intensity to the absorption at 2090 cm^{-1} with the increase of the Cu/Zn
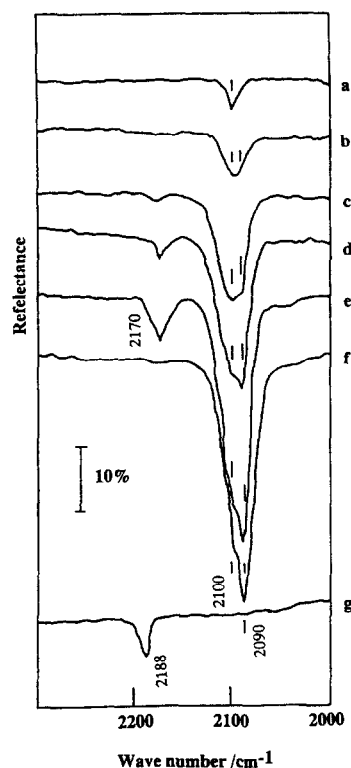

Fig. 9. FT-IR spectra of CO adsorbed on various Cu/ZnO catalysts prepared by method A. Cu/Zn ratios: (a) 100/0; (b) 90/10; (c) 70/30; (d) 50/50; (e) 30/70; (f) 10/90; (g) 0/100.

ratio up to 90/10. Comparing these with the ratio $V_\alpha/(V_\alpha + V_\beta)$ in Fig. 7, one is convinced that the α-oxygen species formed on the steps, corners and/or defects sites of the Cu surface, corresponding to CO adsorption at 2100 cm^{-1}, while the β-oxygen species formed on the flat sites of the Cu surface, corresponding to CO adsorption at 2090 cm^{-1}.

Shriver et al. [47,48] demonstrated that the reaction between metal carbonyls such as $Fe_2(CO)_9$ and $Ru_3(CO)_{12}$ and Lewis acids such as $AlCl_3$ and BF_3, results in the red shift of the CO bands. The bifunctional chemisorption of CO on conventional Rh–Mn, Rh–Ti, Rh–Fe, Rh–Zr and Ru–Co/SiO$_2$ catalysts, also leads to a similar red shift of CO bands [49–51]. Klier et al. [52–54] studied the structures and the morphology of the Cu/ZnO catalysts by PXRD, scanning transmission electron microscopy (STEM) and diffuse reflectance. They found

that noncrystallite Cu dissolved in ZnO on the Cu/ZnO catalysts with Cu/Zn the ratios of 80/20 to 15/85. Here, the 2170 cm^{-1} band showed approximately a 20 cm^{-1} red shift, comparing the fundamental adsorption of CO on ZnO, which may arise from η^2-CO bonding on the Cu–Zn^{2+} sites of S$_{A7-A3}$-derived catalysts.

There has been extensive research on Cu/ZnO-based methanol synthesis/water–gas shift catalysts [5,10,55–59], but the nature of the active center still remains controversial. The ICI groups et al. [10,55,56] claimed that the principal active site for these reactions is on a particle of copper metal. However, several researchers [5,6,60–64] stimulated much interest with their proposal that isolated Cu$^+$ species dissolved in, or supported on, the ZnO phase was the key element. Campbell et al. [65–67] have recently measured methanol synthesis and reverse water–gas shift from CO$_2$ and H$_2$ mixtures on copper model catalysts, inferring structural sensitivity and the principal active site of metallic Cu for these reactions on the Cu/ZnO catalysts. Here, steam reforming of methanol is the reverse reaction of methanol synthesis from CO$_2$, and closely related to reverse water–gas shift. The Cu surface structure and surface area of Cu/ZnO catalysts were measured by the TPO with N$_2$O. In this context, the principal active site of the Cu/ZnO catalyst is regarded as steam reforming of methanol. In Table 2, it is observed that H$_2$ rate or methanol conversion increases with increasing metallic Cu surface area. This is an indication that the catalytic activity depends on metallic Cu surface area alone. The TOF for the Zn-free catalyst is higher than that of any of the binary Cu/ZnO catalysts by a factor of between 2 and 5. This is consistent with the inference that metallic Cu surface catalyze steam reforming of methanol. However, for Cu/ZnO catalysts, a disproportionate relationship exists between the amount of α-oxygen species (V_α), the amount of β-oxygen species (V_β) or the ratio of $V_\alpha/V_\alpha + V_\beta$, against the turnover frequency of H$_2$ (not shown). Namely, the TOF does not correlate with either

the total metallic Cu surface area, the area of metallic Cu step or defect sites, or the area of metallic Cu terrace sites. Nakamra et al. [68] claim that the Zn is actually poisoning the metallic Cu slightly, from the model catalyst of the Zn-deposited polycrystalline Cu surface with Zn coverage above $\theta_{Zn} = 0.17$, catalyzing methanol synthesis. Nix et al. [69] reported that the reducibility of ZnO is substantially enhanced in the presence of metallic Cu, which is clearly evident following treatment in H$_2$ at temperatures exceeding 523 K. In the present experimental condition, the surface ZnO of Cu/ZnO catalyst could be partly reduced to Zn as surface metallic Cu appearing, proposing the surface Zn atoms which poison the surface metallic Cu. These patterns borne out the variety of the TOF with Cu/Zn ratio of Cu/ZnO catalysts, as listed in Table 2. We predict that the TOF should accurately correlate with the surface Cu/Zn atomic ration of Cu/ZnO catalysts. But, because of the difficulty for precise measurement of the surface Zn atoms, it does not prove feasible to extract direct correlation between the TOF and the surface Cu/Zn atomic ratio.

4. Summary

Steam reforming of methanol, CH$_3$OH + H$_2$O $\rightarrow$ CO$_2$ + 3H$_2$, was carried out on various Cu/ZnO catalysts derived from precursors prepared by one of two addition rates of a mixed Cu(NO$_3$)$_2$/Zn(NO$_3$)$_2$ solution to a NaHCO$_3$ solution. The precursors and their reduced products were characterized by PXRD, DTA, TGA, FT-IR, UV, TPO with N$_2$O and CO chemisorption. Based on the analyses of the results, we concluded as follows: (1) The addition rate affects the local concentrations of copper and zinc cations, resulting in the observed difference in the formation of the intermediate, such as amorphous copper hydroxycarbonate and sodium zinc carbonate. This is reflected in the final composition of the precipitates, such as

malachite, aurichalcite and hydrozincite. (2) The α- and β-peaks of the TPO run resulted from the oxidation of the metallic Cu surface having steps, corners and/or defect sites and flat sites, respectively, corresponding to CO chemisorption at 2100 and 2090 cm^{-1}, respectively. The average crystallite sizes of Cu, estimated from the total amount of α- and β-peaks, agreed well with those determined by PXRD. (3) The Cu/ZnO catalysts showed the activity of steam reforming of methanol to vary with composition. This activity originates from metallic Cu surface.

References

[1] H. Kobayashi, N. Takezawa, C. Minochi, J. Catal. 69 (1981) 487.

[2] M. Shimokawabo, N. Takezawa, H. Kobayashi, Appl. Catal. 2 (1982) 379.

[3] N. Takezawa, H. Kobayashi, A. Hirose, M. Shimokawabo, K. Takahashi, Appl. Catal. 4 (1982) 127.

[4] N. Takezawa, H. Kobayashi, Y. Kamega, M. Shimokawbo, Appl. Catal. 3 (1982) 381.

[5] R.G. Herman, K. Klier, G.W. Simmons, B.P. Finn, J.B. Bulko, T.P. Kobylinski, J. Catal. 56 (1979) 407.

[6] Y. Okamoto, K. Fukino, T. Imanaka, S. Teranishi, J. Phys. Chem. 87 (1983) 3740.

[7] P.B. Himelfarb, G.W. Simmons, K. Klier, R.G. Herman, J. Catal. 93 (1985) 442.

[8] P. Porta, S. De Rossi, G. Ferraris, M. Lo Jacono, G. Minelli, G. Moretti, J. Catal. 109 (1988) 367.

[9] P. Porta, G. Fierro, M. Lo Jacono, G. Moretti, Catal. Today 2 (1988) 675.

[10] D. Waller, D. Stirling, F.S. Stone, M.S. Spencer, Faraday Discuss. Chem. Soc. 87 (1989) 107.

[11] G. Sengupta, D.P. Das, M.L. Kundu, S. Dutta, S.K. Roy, R.N. Sahay, K.K. Mishira, Appl. Catal. 5 (1989) 165.

[12] G.-C. Shen, S.I. Fujita, N. Takezawa, J. Catal. 138 (1992) 754.

[13] X-ray Powder Data File, ASTM 10-399.

[14] X-ray Powder Data File, ASTM 19-1458.

[15] X-ray Powder Data File, ASTM 17-743

[16] X-ray Powder Data File, ASTM 10-399, Acta Crystallogr. 4 (1951) 200.

[17] M.H. Stacey, M. Shannon, in: P. Barret, L.C. Dufour (Eds.), Reactivity of Solids, Elsevier, Amsterdam, 1985. p. 713.

[18] J.L. Jambor, Geol. Surv. Canad., Report of Activities, Part C, Paper 76-1C, 1976.

[19] R.D. Shannon, Acta Crystallogr. A 32 (1976) 751.

[20] J.D. Dunitz, L.E. Orgel, Nature 179 (1957) 462.

[21] S. Ghose, Acta Crystallogr. 17 (1964) 1051.

[22] X-ray Power Data File, ASTM 18-1095.

[23] A.F. Wells, Acta Crystallogr. 4 (1951) 200.

[24] J.L. Jambor, G. Pouliot, Can. Mineral. 8 (1965) 385.

[25] E.B.M. Doesburg, R.H. Hoppener, B. de Koning, X.D. Xu, J.J.F. Scholten, Stud. Surf. Sci. Catal. 31 (1987) 767.

[26] R.G. Herman, C.E. Bogdan, Mater. Chem. Phys. 35 (1987) 233.

[27] Dana's System of Mineralogy, 7th ed., vol. 2, Wiley, New York, 1951, p. 247.

[28] K.A. Alwan, J.H. Thomas, P.A. Williams, Trans. Met. Chem. 5 (1980) 3.

[29] X-ray Powder Data File, ASTM 1-457.

[30] S.I. Fujita, A.M. Satriyo, G.-C. Shen, N. Takezawa, Catal. Lett. 25 (1994) 29.

[31] B. Dvorak, J. Pasek, J. Catal. 18 (1970) 108.

[32] M.J. Luys, P.H. van Oeffelt, P. Pierters, R. ter Veen, Catal. Today 10 (1991) 283.

[33] K. Narita, N. Takezawa, H. Kobayashi, I. Toyoshima, React. Kinet. Catal. Lett. 19 (1982) 91.

[34] F.H.P.M. Habraken, E.Ph. Kieffer, G.A. Bootsma, Surf. Sci. 83 (1979) 45.

[35] F.H.P.M. Habraken, C.M.A. Mesters, G.A. Bootsma, Surf. Sci. 97 (1980) 264.

[36] J.W. Evans, M.S. Wainwright, A. Bridgewater, D.J. Young, Appl. Catal. 7 (1983) 75.

[37] G.J.J. Bartley, R. Burch, R.J. Chappell, Appl. Catal. 43 (1988) 91.

[38] M.J. Luys, P.H. van Oeffelt, W.G.J. Brouwer, A.P. Pijpers, J.J.F. Scholten, Appl. Catal. 46 (1989) 161.

[39] J.J.F. Scholten, J.A. Konvalinka, Trans. Faraday Soc. 65 (1969) 2465.

[40] G. Sengupta, D.K. Gupta, M.L. Kundu, S.P. Sen, J. Catal. 67 (1981) 223.

[41] G.C. Chinchen, C.M. Hay, H.D. Vandervell, K.C. Waugh, J. Catal. 103 (1987) 79.

[42] G.L. Griffin, J.T. Yates Jr., J. Chem. Phys. 77 (1982) 3751.

[43] J. Pritchard, T. Catterick, R.K. Gupta, Surf. Sci. 53 (1975) 1.

[44] K. Horn, J. Pritchard, Surf. Sci. 55 (1976) 701.

[45] K. Korn, M. Hussain, J. Pritchard, Surf. Sci. 63 (1977) 224.

[46] P. Hollins, K.J. Davies, J. Pritchard, Surf. Sci. 138 (1984) 75.

[47] S.B. Butts, E.M. Holt, S.H. Strauss, N.W. Alcock, R.E. Stimson, D.F. Shriver, J. Am. Chem. Soc. 101 (1979) 5864.

[48] F. Correa, R. Nakamura, R.E. Stimson Jr., R.L. Burwell, D.F. Shriver, J. Am. Chem. Soc. 102 (1980) 5112.

[49] A. Fukuoka, T. Kimura, N. Kosugi, H. Kuroda, Y. Minai, Y. Sakai, T. Tominaga, M. Ichikawa, J. Catal. 126 (1990) 434.

[50] F.-S. Xiao, A. Fukuoka, M. Ichikawa, J. Catal. 126 (1990) 434.

[51] M. Ichikawa, T. Fukushima, J. Phys. Chem. 89 (1985) 1564.

[52] S. Mehta, G.W. Simmons, K. Klier, R.G. Herman, J. Catal. 57 (1979) 339.

[53] J.M. Dominquez, G.W. Simmons, K. Klier, J. Mol. Catal. 20 (1983) 369.

[54] J.B. Bulko, R.G. Herman, K. Klier, G.W. Simmons, J. Phys. Chem. 83 (1979) 3118.

[55] G.C. Chinchen, K.C. Waugh, D.A. Whan, Appl. Catal. 25 (1986) 101.

[56] G.C. Chinchen, P.J. Denny, D.G. Parker, M.S. Spencer, D.A. Whan, Appl. Catal. 30 (1987) 333.

[57] G. Liu, D. Wilcox, M. Garland, H.H. Kung, J. Catal. 90 (1984) 139.

[58] J.S. Lee, K.H. Lee, S.Y. Kim, J. Catal. 144 (1985) 414.

[59] M. Muhler, E. Tornqvist, L.P. Nielsen, B.S. Clausen, H. Topsoe, Catal. Lett. 25 (1994) 1.

[60] K.G. Chanchlani, R.R. Hudgins, P.L. Silveston, J. Catal. 136 (1992) 59.

[61] Y. Kanai, T. Watanabe, T. Fujitani, M. Saito, J. Nakamura, T. Uchijima, Catal. Lett. 27 (1994) 67.

[62] V. Ponec, Catal. Lett. 11 (1991) 249.

[63] K. Klier, Adv. Catal. 31 (1982) 243.

[64] K. Klier, Appl. Surf. Sci. 19 (1984) 267.

[65] K.H. Ernst, C.T. Campbell, G. Moretti, J. Catal. 134 (1992) 66.

[66] J. Yoshihara, S. Parker, A. Schafer, C.T. Campbell, Catal. Lett. 31 (1985) 313.

[67] J. Yoshihara, C.T. Campbell, J. Catal. 161 (1996) 776.

[68] J. Nakamura, I. Nakamura, T. Uchijima, Y. Kanai, T. Watanable, M. saito, T. Fujitani, J. Catal. 160 (1996) 65.

[69] D.S. King, R.M. Nix, J. Catal. 160 (1996) 76.